Flux-tunable supercurrent in full-shell nanowire Josephson junctions

G. Giavaras* and R. Aguado†

Instituto de Ciencia de Materiales de Madrid (ICMM), Consejo Superior de Investigaciones Cientficas (CSIC), Sor Juana Inés de la Cruz 3, 28049 Madrid, Spain

(Received 11 May 2023; revised 14 November 2023; accepted 7 December 2023; published 11 January 2024)

Full-shell nanowires formed by a semiconducting core fully wrapped by an epitaxial superconducting shell, have recently been introduced as promising hybrid quantum devices. Despite this, however, their properties when forming a Josephson junction (JJ) have not been elucidated yet. We here fill this void by theoretically studying the physics of JJs based on full-shell nanowires. In the hollow-core limit, where the thickness of the semiconducting layer can be ignored, we demonstrate that the critical supercurrent I^c can be tuned by an external magnetic flux Φ. Specifically, $I^c(\Phi)$ *does not follow* the Little-Parks modulation of the superconducting pairing $\Delta(\Phi)$ and exhibits steps for realistic values of nanowire radii. The position of the steps can be understood from the underlying symmetries of the orbital transverse channels contributing to the supercurrent.

DOI: 10.1103/PhysRevB.109.024509

I. INTRODUCTION

The experimental demonstration of hybrid semiconductor-superconductor Josephson junctions (JJs) [1–9] has spurred a great deal of research uncovering new physics of Andreev bound states (ABSs) [10], including their spin splitting and spin-orbit (SO) coupling effects [11–14] as well as their microwave response [14–17]. Moreover hybrid semiconductor-superconductor JJs are being explored for novel qubit applications [18] such as gate-tunable transmon qubits [19–23], Andreev qubits [24,25], and parity-protected qubits [26,27]. From a different perspective, compatibility with high magnetic fields and gate tunability hold promise for demonstrating topological quantum computing based on Majorana zero modes [28–30].

Full-shell nanowires (NWs), where a semiconducting core fully coated by a superconductor [31] and threaded by an external magnetic flux Φ, have recently been explored as a powerful platform to generate Majorana zero modes [32–35]. Their interest, however, goes beyond Majorana physics since the full-shell geometry gives rise to a great deal of new physics, including nontrivial Φ-dependent superconductivity [36] owing to the Little-Parks (LP) effect [37,38], as well as analogs of subgap states in vortices [39,40].

While JJs based on full-shell NWs start to attract experimental attention [22,23,41,42], a theoretical understanding is lacking. The purpose of the present work is to fill this void by studying superconductor-normal-superconductor (SNS) junctions based on hollow-core full-shell NWs [Fig. 1(a)]. Our main result is the demonstration of critical supercurrent, I^c, tunability as a function of Φ [Fig. 1(b)]. We find a stepwise decrease with Φ-dependent features which can be analytically understood in terms of the underlying orbital degeneracies and symmetries of the ABS spectrum. The Φ-dependence of the critical supercurrent reported here is *completely unrelated* to the LP modulation of the superconducting pairing, and can be observed even when there is no LP modulation. In stark contrast to previously reported flux-induced supercurrents which are LP-dominated [23,43].

Our findings could have important implications in recently proposed transmon qubit designs [23]. Specifically the flux tunability could offer further functionalities. These include, for example, tuning the Josephson potential as well as the corresponding anharmonicity of the qubit with the applied magnetic flux. An experimental demonstration of the stepwise flux dependence of the critical supercurrent would be an irrefutable proof of high control over the individual modes (ABSs) in the SNS junction by simply tuning the applied flux. The stepwise dependence could also implicitly reflect a sample of sufficient quality that could be then utilized to define qubits. In addition, the ability to address individual modes could allow one to probe the topological regime and Majorana bound states using as a platform JJs.

In Sec. II, we present the physical model of the full-shell nanowire and the Josephson junction. In Sec. III, we present the main results for the flux tunable critical current, and then develop a simplified junction model in Sec. IV. Our conclusions are given in Sec. V. Appendix A details how the pairing potential is modified by the flux due to the Little-Parks effect. In Appendix B, the critical current is examined in the presence of a spatially modulated chemical potential along the junction. In Appendix C, we present various results for the critical current using a simplified SNS junction model. In Appendix D, we study the current in a junction with a reduced transparency. Finally, spin-orbit coupling effects are briefly explored in Appendix E.

II. PHYSICAL MODEL

A. Nanowire Hamiltonian

We first consider a cylindrical semiconducting NW, unit vectors $(\hat{e}_r, \hat{e}_\varphi, \hat{e}_z)$, in the presence of a magnetic field

*g.giavaras@gmail.com
†ramon.aguado@csic.es

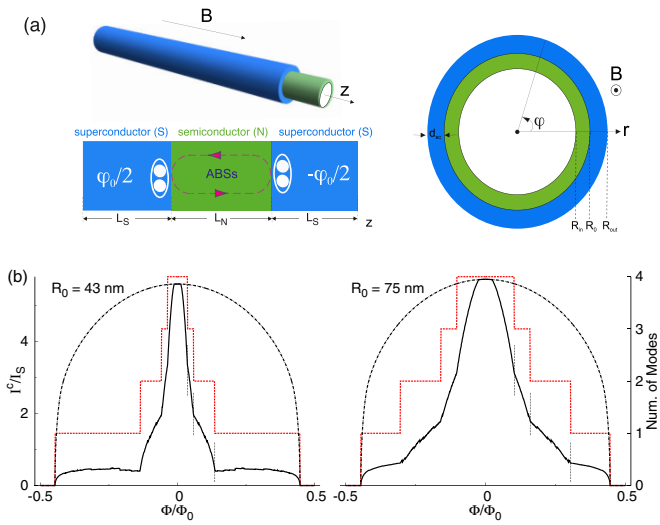

FIG. 1. (a) (Left) Schematics of a semiconducting NW (green) fully coated by a superconducting shell (blue) and threaded by a longitudinal magnetic field B. (Right) The cross section defines an insulating region (white) of radius $R_{\rm in}$, a semiconducting layer of thickness $d_{\rm semi} = R_0 - R_{\rm in}$ and a superconducting shell of thickness $d_{\rm sc} = R_{\rm out} - R_0$. Within the hollow-core approximation [32], the thickness of the semiconducting layer is $d_{\rm semi} \approx 0$. This fixes the radial coordinate $r = R_0$ and the magnetic flux $\Phi = \pi R_0^2 B$. (Bottom) Schematics of an SNS junction where a normal (N) region of length L_N is encapsulated between two superconducting (S) regions of length L_S and phase difference φ_0. (b) Flux-tunable critical current $I^{\rm c}$ (solid curves left axis, in units of $I_S = e\Delta_0/\hbar$) and number of nondegenerate subgap modes (dotted lines, right axis) within the zeroth lobe, $n = 0$. By increasing the flux the number of modes contributing to $I^{\rm c}$ decreases at each vertical line, "kink" point, resulting in a stepwise current profile. Dash-dotted curves show $I^{\rm c}(\Phi) = I^{\rm c}(0)\Delta(\Phi)/\Delta_0$. $n \neq 0$ lobes exhibit similar characteristics.

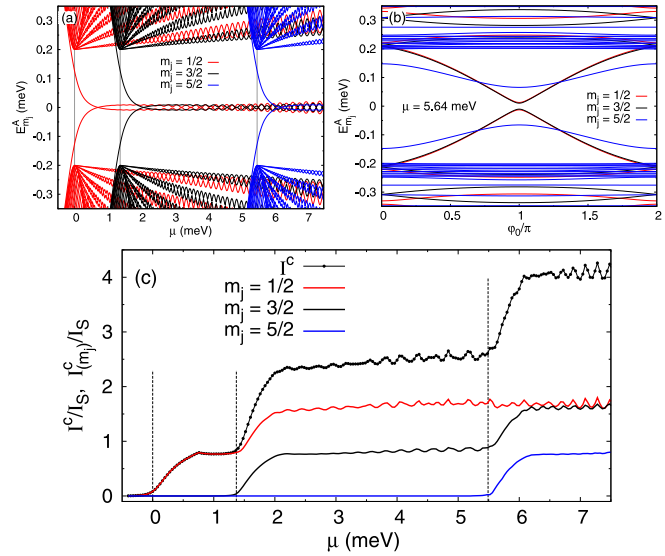

FIG. 2. (a) Zero-flux energies of $H_A(m_j)$ as a function of chemical potential at $\varphi_0 = \pi$ with $E^A_{-m_j} = -E^B_{m_j}$ and $E^B_{m_j} = E^A_{m_j+1}$. As μ increases the vertical lines define $V_1^0(m_j) \approx 0$ for $m_j = 1/2, 3/2, 5/2$ respectively. The oscillatory dependence around $E^A_{m_j} = 0$ is generic in junctions governed by the BdG equation. (b) Energies of $H_A(m_j)$ as a function of φ_0. There are five positive subgap levels: $E^A_{1/2}$, $E^B_{1/2} = E^A_{3/2}$ and $E^B_{3/2} = E^A_{5/2}$. Any other pair of levels has a nonzero spacing while the degeneracies are lifted for $\alpha \neq 0$. (c) Critical current, $I^{\rm c}$, and m_j contributions $I^{\rm c}_{(m_j)} = I^{\rm c}_{-m_j} + I^{\rm c}_{m_j}$. Vertical lines are the same as in (a). Parameters: $L_S = 2000$ nm, $L_N = 100$ nm, $R_0 = 43$ nm, $\alpha = 0$, $\Delta = \Delta_0 = 0.2$ meV, and $I_S = e\Delta_0/\hbar$.

$\vec{B} = B\hat{e}_z$ and SO coupling. Within the hollow-core approximation [32], the electrons are strongly confined near the surface of the NW. We can therefore fix the radial coordinate $r = R_0$ [Fig. 1(a)], thus the flux threading the NW is $\Phi = \pi B R_0^2$ and the vector potential is $\vec{A} = A_\varphi \hat{e}_\varphi = \frac{\Phi}{2\pi R_0}\hat{e}_\varphi$. The Hamiltonian is then

$$H_0(\vec{A}) = \frac{(\vec{p} + eA_\varphi \hat{e}_\varphi)^2}{2m^*} - \mu + H_{\rm SO}, \tag{1}$$

with $\vec{p} = (p_\varphi, p_z) = (-\frac{i\hbar}{R_0}\partial_\varphi, -i\hbar\partial_z)$ being the momentum operator, m^* the effective mass and μ the chemical potential. Assuming radial inversion symmetry breaking, namely, $\vec{\alpha} = \alpha\hat{e}_r$, the Rashba SO Hamiltonian is [44] $H_{\rm SO} = H^z_{\rm SO} + H^\perp_{\rm SO} = \frac{\alpha}{\hbar}[p_z\sigma_\varphi - (p_\varphi + eA_\varphi)\sigma_z]$, with the spin-1/2 Pauli matrices $\sigma_\varphi = \sigma_y\cos(\varphi) - \sigma_x\sin(\varphi)$, σ_z and the SO coupling α.

Owing to the proximity effect the semiconducting core acquires superconducting pairing terms. These are modulated by Φ through the LP effect, which induces a winding of the superconducting phase in the shell around the NW axis $\mathbf{\Delta} = \Delta e^{in\varphi}$. Here, we assume that the coupling between the semiconductor and the superconductor is strong, such that the proximity-induced pairing terms in the semiconductor inherit the LP effect of the superconducting shell. The amplitude Δ and the winding number n (fluxoid) depend implicitly on Φ (Appendix A). Defining the normalized flux $n_\Phi = \Phi/\Phi_0$, where $\Phi_0 = h/2e$, then $n = \lfloor n_\Phi \rceil$. Thus, deviations from integer fluxes are measured through the variable $\phi = n - n_\Phi$, with $\phi = 0$ corresponding to the middle of a so-called LP lobe [36]. In what follows, we set $\Delta(\Phi = 0) \equiv \Delta_0$.

In the Nambu basis $\Psi = (\psi_\uparrow, \psi_\downarrow, \psi^\dagger_\downarrow, -\psi^\dagger_\uparrow)$, the Bogoliubov-de-Gennes (BdG) Hamiltonian $H_{\rm BdG}$ is decomposed in one-dimensional models [5,44–47] labelled in terms of the eigenvalues m_j of a generalized angular momentum operator [32] $\hat{J}_z(n) = -i\partial_\varphi + \frac{1}{2}\sigma_z + \frac{1}{2}n\tilde{\tau}_z$, with $\tilde{\tau}$ acting in Nambu space. Acceptable wave functions require that [32] $m_j = \pm 1/2, \pm 3/2, \ldots$ for even n and $m_j = 0, \pm 1, \ldots$ for odd n. The resulting BdG Hamiltonians[1] are

$$H_{\rm BdG} = \begin{pmatrix} H_A & H^z_{\rm SO} \\ -H^z_{\rm SO} & H_B \end{pmatrix}, \tag{2}$$

with $H^z_{\rm SO} = -\alpha\partial_z\tilde{\tau}_z$, and

$$H_A = \begin{pmatrix} \frac{p_z^2}{2m^*} + V_1 & \Delta \\ \Delta^* & -\frac{p_z^2}{2m^*} + V_2 \end{pmatrix}. \tag{3}$$

[1]Without SO coupling and LP effect, Eq. (2) reduces to the model used in Ref. [5] to study supercurrent interference in JJs based on cylindrical semiconducting NWs. Without pairing Eq. (2) is the BdG analog of the model used to study conductance oscillations in semiconducting core-shell NWs [44–47].

H_B is obtained by substituting $V_1 \to V_3$, $V_2 \to V_4$, with ($\hbar = 1$)

$$V_{1(2)}(\phi) = V^0_{1(2)} + \delta^+_{m_j}(\phi) \pm \frac{1}{8m^*R_0^2}\phi^2,$$
$$V_{3(4)}(\phi) = V^0_{3(4)} + \delta^-_{m_j}(\phi) \pm \frac{1}{8m^*R_0^2}\phi^2. \quad (4)$$

At $\phi = 0$, the potentials are

$$V^0_{1(3)} = -\mu + \frac{(1 \mp 2m_j)^2}{8m^*R_0^2} + \frac{(1 \mp 2m_j)\alpha}{2R_0}, \quad (5)$$

with $V^0_2 = -V^0_1$ and $V^0_4 = -V^0_3$. Small deviations from integer fluxes ($\phi = 0$) are captured by the linear terms

$$\delta^{\pm}_{m_j}(\phi) = \frac{-2m_j \pm 1}{4m^*R_0^2}\phi \pm \frac{\alpha}{2R_0}\phi. \quad (6)$$

At $\phi = 0$, the terms $V^0_1(m_j)$ and $V^0_3(m_j)$ govern the chemical potential at which the energy levels of H_A and H_B respectively cross zero energy with the important quantity being the difference $V^0_3(m_j) - V^0_1(m_j) = m_j/m^*R_0^2 + 2m_j\alpha/R_0$. When $\alpha = 0$ the energy levels of $H_A(m_j + 1)$ and $H_B(m_j)$ are degenerate $[V^0_1(m_j + 1) = V^0_3(m_j)]$, therefore, energy levels belonging to different m_j numbers cross zero energy simultaneously.

B. SNS junction

The SNS junction is defined by a spatial dependence of the pairing potential, namely, $\Delta_{R/L} = \Delta e^{i(n\varphi \pm \varphi_0/2)}$, where φ_0 is the superconducting phase difference and R/L denotes the right/left superconducting (S) region of length L_S. The normal (N) region is defined as $\Delta_N = 0$ within a length L_N [48]. For simplicity, we assume in the main text that μ is spatially independent (uniform) along the z direction. In a realistic experimental implementation, however, the superconducting full shell is expected to screen any external electric field making gating only effective in the N region. This configuration can be modelled as a smooth spatial variation of the chemical potential in the N region (Appendix B). A uniform chemical potential results in the maximum critical current, whereas the critical current is reduced as the potential offset between the N and S regions increases.

Assuming zero temperature the supercurrent-phase relationship $I(\varphi_0)$ is written in terms of m_j contributions

$$I(\varphi_0) = \sum_{m_j} I_{m_j}(\varphi_0) = -\frac{e}{\hbar}\sum_{m_j}\sum_{k>0}\frac{dE_{k,m_j}}{d\varphi_0}, \quad (7)$$

where E_{k,m_j} are the positive BdG eigenvalues. These are computed by discretizing the SNS junction on a lattice with a uniform spacing using the method of finite-differences. The continuum BdG eigenvalue problem is thus transformed to a matrix eigenvalue problem which is solved by standard numerical routines. The critical current is $I^c = \max[I(\varphi_0)]$ and its absolute value within $[0, \pi]$ can be decomposed into m_j contributions $I^c_{m_j}$.

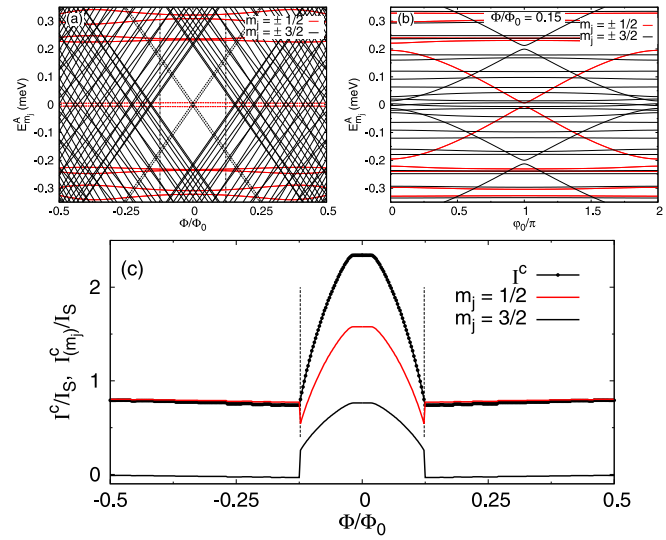

FIG. 3. (a) Energies of $H_A(m_j)$ as a function of flux at $\varphi_0 = \pi$ with $E^A_{-m_j} = -E^B_{m_j}$ and $E^B_{m_j} = E^A_{m_j+1}$. Dotted lines correspond to anticrossing points. Vertical lines define the flux, $\Phi/\Phi_0 \approx \pm 0.125$, where the contribution of a subgap mode of $H_B(m_j)$ or $H_A(m_j + 1)$ is suppressed. (b) Energies of $H_A(m_j)$ as a function of φ_0 at $\Phi/\Phi_0 = 0.15$. (c) Critical current, I^c, and m_j contributions $I^c_{(m_j)} = I^c_{-m_j} + I^c_{m_j}$. Vertical lines are the same as in (a). Parameters: $L_S = 2000$ nm, $L_N = 100$ nm, $R_0 = 43$ nm, $\alpha = 0$, $\Delta = \Delta_0 = 0.2$ meV, $\mu = 2.5$ meV, and $I_S = e\Delta_0/\hbar$.

III. FLUX TUNABLE CRITICAL CURRENT

We start the analysis of the SNS junction by focusing on the zero-flux case $\Phi = 0$. As shown in Fig. 2(a), by increasing the chemical potential BdG levels are induced in a systematic way in the superconducting gap when $V^0_1(m_j) \approx 0$. Because of the relatively small N region, $L_N = 100$ nm, each of $H_A(m_j)$ and $H_B(m_j)$ contributes one subgap level (mode). The degree of φ_0-dispersion depends on the exact value of μ, and some subgap levels can be quasidegenerate [Fig. 2(b)]. A smooth potential barrier $\mu(z)$ on top of the global potential μ allows us to precisely control the number of active modes in the junction by depleting the N region (Appendix B).

The critical current is plotted in Fig. 2(c). A noticeable increase in the current is observed when an extra BdG level shifts into the superconducting gap. Small current fluctuations, which are more pronounced at larger chemical potentials μ, are due to small energy variations at $E^A_{m_j} \approx 0$ [Fig. 2(a)]. The details of the current profile depend on the characteristic length scale of the SNS junction (R_0, L_S, L_N).

We proceed to study finite flux effects for an SNS junction governed by Eq. (2). At small fluxes the linear terms $\delta^{\pm}_{m_j}(\phi)$ [Eq. (6)] are the dominant ones and shift the zero-flux energies. The main physics is illustrated in Fig. 3(a), where we plot the energies of $H_A(m_j)$ when only $m_j = 1/2, 3/2$ are relevant. The key feature is that by increasing Φ the $\Phi = 0$ subgap levels which anticross ($\varphi_0 = \pi$, $E^A_{m_j} \approx 0$) shift in the quasicontinuum. Although, these levels still anticross when $\Phi \neq 0$, the anticrossing point gradually shifts outside the gap. In Fig. 3(b), the anticrossing lying outside the gap is due to $E^B_{1/2}$,

$E^A_{3/2}$, $[\delta^-_{1/2}(\phi) = \delta^+_{3/2}(\phi) \neq 0]$ whereas the anticrossing lying in the gap is due to $E^A_{1/2}$ for which $\delta^+_{1/2}(\phi) = 0$. The required flux to suppress the contribution of a subgap mode of $H_B(m_j)$ or $H_A(m_j + 1)$ is of the order of $(2m_j + 1)|\phi| \approx 4\Delta m^* R_0^2$, therefore, larger m_j subgap modes are suppressed at smaller fluxes. This simplified approach assumes that μ is large enough so that the corresponding anticrossing lies at zero energy. In Fig. 3(c), $\Phi/\Phi_0 \approx \pm 0.125$ defines a crossover, kink point, which is formed when a subgap mode is suppressed and then the current versus flux drops at a smaller overall rate. For the example in Fig. 3(c) $\delta^+_{1/2}(\phi) = 0$, so this rate is zero but as shown below the physics is more interesting for larger m_j.

We now include the LP modulation (Appendix A) $\Delta = \Delta(n, \Phi, R_0, d_{sc}, \xi)$, where ξ is the coherence length of the superconducting shell. When the shell thickness is vanishingly small, $d_{sc} \to 0$, then Δ depends on ϕ instead of Φ/Φ_0. We consider a destructive regime in which $\Delta = 0$ near the boundaries of the lobes and $\Delta = \Delta_0$ at the center of the lobes [Fig. 4(a)].

In Fig. 4, the current at $\phi = 0$ ($\Phi/\Phi_0 = 0, 1$) depends on μ which specifies the number and position of subgap modes in the superconducting gap. By varying ϕ with respect to $\phi = 0$ the current is gradually reduced, and a kink point is formed at the flux where the contribution of a mode vanishes. The current for $n = 1$ exhibits similar characteristics to that for $n = 0$ but with noticeable differences, e.g., the $\phi = 0$ currents in the two lobes are different even when Δ is the same. The reason is the different potentials $V_{1(2)}$ in the BdG Hamiltonian. According to Fig. 4, the flux dependence of Δ cannot be used to explain $I^c(\Phi)$. The *formula* [23,43] $I^c(\Phi) \approx I^c(\Phi = 0)\Delta(\Phi)/\Delta_0$ completely fails to capture the correct flux dependence of I^c in the multimode regime.[2] Instead, a good *approximation* to the current is obtained by assuming the approximate flux dependence of the BdG levels, $E_{m_j}(\phi) \approx E_{m_j}(\phi = 0)\Delta(\phi)/\Delta_0 + \delta^{\pm}_{m_j}(\phi)$, with $E_{m_j}(\phi = 0)$ being the exact $\phi = 0$ BdG levels, and using Eq. (7) with all positive levels included. When the terms $\delta^{\pm}_{m_j}(\phi)$ become smaller, e.g., by increasing R_0, the kink points shift at higher fluxes [Fig. 1(b)].

IV. SIMPLIFIED SNS JUNCTION MODEL

The approximate results in Fig. 4 reveal the vital role of the linear terms $\delta^{\pm}_{m_j}(\phi)$. To obtain further *qualitatively* insight into the physics we develop a simplified model where the supercurrent $I(\varphi_0)$ is based on the ABSs:

$$E_{\pm,k}(\varphi_0, \Phi) = \pm \Delta(\Phi)\sqrt{1 - \tau_k \sin^2(\varphi_0/2)} + w_k \frac{\Phi}{\Phi_0}, \tag{8}$$

$k = 1, 2, \ldots, M$ is the number of ABSs and the parameters $0 < \tau_k \leqslant 1$ model the transparency of the SNS junction. The linear terms $w_k \Phi/\Phi_0$ with $w_k = (k - 1)/2m^* R_0^2$ play the same role as $\delta^+_{m_j}(\phi)$ [Eq. (6)] for $\alpha = 0$ (Appendix C). We emphasize that the exact φ_0 dispersion is not important and we employ Eq. (8) to demonstrate the crossover from the LP to the stepwise regime.

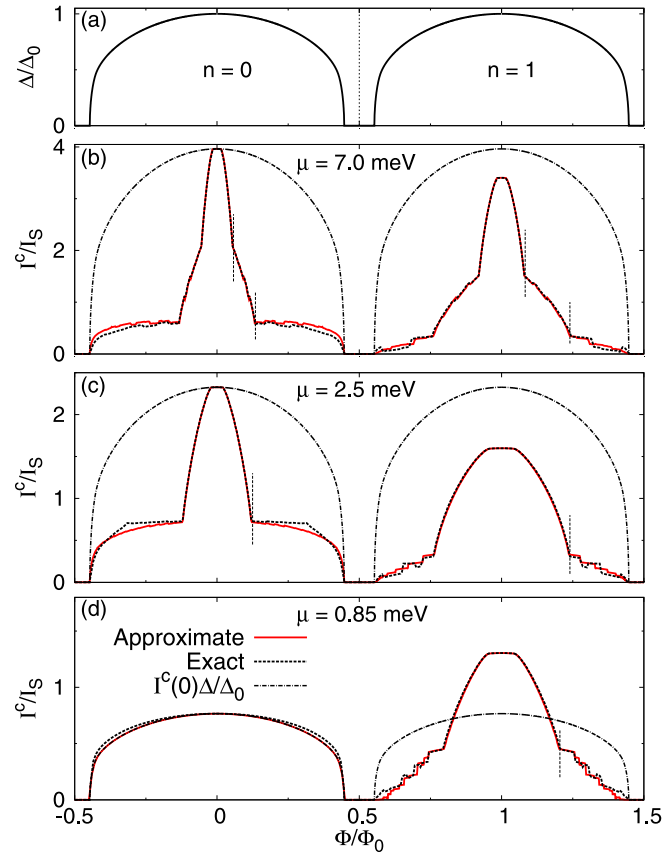

FIG. 4. (a) Pairing potential versus flux for lobes $n = 0$ and $n = 1$. [(b)–(d)] Exact and approximate currents calculated with Δ as in (a). Vertical lines indicate kink points where the number of nondegenerate subgap modes decreases by one. For $n = 0$, $\mu = 7$ meV, and $\Phi = 0$, there are three subgap modes coming from $m_j = 1/2$, 3/2, 5/2. For $\Phi \neq 0$, two kink points are formed when $E^A_{5/2}$ and $E^A_{3/2}$ shift successively outside the gap. For $n = 0$, $\mu = 2.5$ meV, and $\Phi = 0$, there are two subgap modes coming from $m_j = 1/2$, 3/2, thus, for $\Phi \neq 0$ one kink point is formed when $E^A_{3/2}$ shifts outside the gap. For $n = 0$, $\mu = 0.85$ meV, the single mode current ($m_j = 1/2$) is LP-dominated because $\delta^+_{1/2} = 0$. For the same reason $E^A_{1/2}$ remains to a good approximation in the gap independent of Φ for any μ. Approximate results for $n = 0$, $\mu = 15$ meV, and $m_j = 1/2$, 3/2, 5/2, 7/2 are shown in Fig. 1(b). Similar arguments are valid for $n = 1$ but now the current is never LP-dominated. At $\Phi = \Phi_0$ and $\mu = 7$ meV, the angular values $m_j = 0$, 1, 2 are relevant while for $\mu = 2.5$, 0.85 meV only $m_j = 0$, 1 are relevant. Because $\delta^+_{m_j} \neq 0$ all modes shift outside the gap leading to a more "noisy" current profile compared to $n = 0$. A weak SO coupling, $\alpha \neq 0$, does not alter the basic characteristics (Appendix E). Parameters: $L_S = 2000$ nm, $L_N = 100$ nm, $R_0 = 43$ nm, $\alpha = 0$, $\Delta_0 = 0.2$ meV, $\xi = 80$ nm, $d_{sc} = 0$, and $I_S = e\Delta_0/\hbar$.

For $\tau_k = 1$ and when all w_k are zero, the analytically computed supercurrent (Appendix C) can be written as $I(\varphi_0) = MI_Z(\varphi_0)$, and for the critical current, we recover the standard result [49,50] $I^c(\Phi) = Me\Delta(\Phi)/\hbar = I^c(0)\Delta(\Phi)/\Delta_0$; here the flux dependence of I^c is due solely to the LP modulation of $\Delta(\Phi)$. A completely different situation occurs when $w_k \neq 0$. Now within the flux range $0 \leqslant$

[2]The agreement for $n = 0$, $\mu = 0.85$ meV stems from $\delta^+_{1/2} = 0$.

$w_k\Phi/\Phi_0 \leqslant \Delta(\Phi)$, we define the phase $\theta_k = \theta_k(\Phi)$ satisfying $E_{-,k}(\theta_k) = 0$ with $0 \leqslant \theta_k \leqslant \pi$. When Φ increases the levels $E_{-,k}(\theta_k)$ shift upwards decreasing $I^c(\Phi)$. A simple inspection indicates that $I^c(\Phi)$ is equal to the larger of $kI_Z(\theta_k)$ and $(k-1)I_Z(\theta_{k-1})$, with $k \to k-1$ as the flux increases. For the flux

$$\frac{\Phi}{\Phi_0} = \Delta(\Phi)\sqrt{\frac{k^2-(k-1)^2}{k^2w_k^2-(k-1)^2w_{k-1}^2}}, \tag{9}$$

the currents satisfy

$$kI_Z(\theta_k) = (k-1)I_Z(\theta_{k-1}), \tag{10}$$

then a kink point is formed and the number of ABSs contributing to $I^c(\Phi)$ decreases by one.[3] Because θ_{k-1} varies with flux slower than θ_k, Eq. (10) leads to a stepwise decrease of $I^c(\Phi)$. For very large R_0 (>150 nm), w_k are vanishingly small and the current steps/kink points are formed at fluxes lying near the boundaries of the lobe, thus $I^c(\Phi)$ is trivially LP-dominated. In contrast, experimentally reported [34,35,42,43] R_0 ($\lesssim$ 100 nm) guarantee a stepwise decrease. In Appendix C, we generalize the simplified SNS junction model to $\tau_k < 1$ and make a connection with the exact BdG model in Appendix D.

V. CONCLUSION

The critical supercurrent in full-shell NW Josephson junctions does not follow the LP modulation and exhibits a stepwise flux dependence. The position of the steps depends on the symmetries of the transverse channels and it is thus gate-tunable. This prediction should be robust for low-disordered NWs especially in the low-flux range, $n = 0$ with $\Phi \lesssim \Phi_0/2$, where interference due to m_j mixing should be negligible. Such effects, similar to Fraunhofer-like interference in diffusive many-channel planar junctions [51] could be of relevance in the first LP lobe, $n = 1$ at $\Phi \approx \Phi_0$, and lead to further structures in I^c. A channel-mixing mechanism which could arise due to interactions, external fields and/or geometry effects is expected to degrade to some degree, but not completely, the stepwise flux dependence. Some experiments have measured supercurrents which are LP-dominated and have shown no signs of a stepwise current profile [23,43]. An enhanced sample quality might be required to reveal the stepwise dependence of the critical current. Further theoretical and experimental studies are needed to clarify the complete physics.

Experiments able to discriminate between the flux modulation of the gap and the subgap structure, for instance, Joule heating experiments [42], could be an interesting platform to explore the predicted effects of our work. Our findings could also be of relevance for transmon qubits in full-shell NWs [23], where the flux tunability of the critical current could lead to novel functionalities. These include, for example, precise control of the ratio of the Josephson coupling to the charging energy governing the qubit anharmonicity.

[3]Because $w_1 = 0$, as happens with $\delta^+_{1/2}$, the current $I_Z(\theta_1)$ should be replaced by $e\Delta(\Phi)/\hbar$ (Appendix C).

ACKNOWLEDGMENTS

This research was supported by Grants No. PID2021-125343NB-I00 and No. TED2021-130292B-C43 funded by MCIN/AEI/10.13039/501100011033, "ERDF A way of making Europe" and European Union Next Generation EU/PRTR. Support by the CSIC Interdisciplinary Thematic Platform (PTI+) on Quantum Technologies (PTI-QTEP+) is also acknowledged.

APPENDIX A: SUPERCONDUCTING PAIRING POTENTIAL

The superconducting pairing potential, Δ, due to the Little-Parks effect [37,38] acquires a flux dependence. If Δ_0 is the value of Δ at $\Phi = 0$ then according to Abrikosov-Gor'kov [52,53] a pair-breaking term Λ results in the following modulation of Δ:

$$\begin{aligned}
\ln\frac{\Delta}{\Delta_0} &= -\frac{\pi}{4}\frac{\Lambda}{\Delta}, \quad \Lambda \leqslant \Delta,\\
\ln\frac{\Delta}{\Delta_0} &= -\ln\left(\frac{\Lambda}{\Delta}+\sqrt{(\Lambda/\Delta)^2-1}\right)\\
&\quad +\frac{\sqrt{(\Lambda/\Delta)^2-1}}{2(\Lambda/\Delta)}\\
&\quad -\frac{\Lambda}{2\Delta}\arctan\frac{1}{\sqrt{(\Lambda/\Delta)^2-1}}, \quad \Lambda \geqslant \Delta.
\end{aligned} \tag{A1}$$

Within a Ginzburg-Landau theory [54–57] the magnetic flux dependence of Λ is given by the approximate expression

$$\Lambda \approx \frac{\xi^2 k_B T_c}{\pi R_0^2}\left[4\left(n-\frac{\Phi}{\Phi_0}\right)^2+\frac{d_{sc}^2}{R_0^2}\left(\frac{\Phi^2}{\Phi_0^2}+\frac{n^2}{3}\right)\right]. \tag{A2}$$

The parameter ξ denotes the coherence length of the superconducting shell which has thickness d_{sc}, n is the lobe index, T_c is the critical temperature at zero flux, and $k_BT_c = \Delta_0/1.76$ [53] where k_B is Boltzmann's constant. In our work, we focus on $R_0 \gg d_{sc}$ and for simplicity we set $d_{sc} = 0$; a small nonzero d_{sc} introduces only minor corrections to the final magnetic flux dependence of Δ. The numerical solution to Eq. (A1) is well-known and can be found in the literature, for example, in Ref. [53]. In the limit $\Lambda \to \Delta_0/2$, the pairing potential nearly vanishes, $\Delta \to 0$, we then set $\Delta = 0$ for $\Lambda \geqslant \Delta_0/2$ to model a destructive regime. One example of the pairing potential for $R = 43$ nm, $\xi = 80$ nm, $d_{sc} = 0$ is shown in Fig. 4(a) of the main text.

APPENDIX B: SNS JUNCTION WITH SPATIALLY DEPENDENT CHEMICAL POTENTIAL

In the main text, the chemical potential, μ, is taken to be constant (spatially independent) along the SNS junction. This configuration simplifies the theoretical analysis but it might be difficult to realize experimentally. For this reason, we consider one more configuration where the chemical potential is spatially dependent, i.e., $\mu = \mu(z)$. In this context, we assume that an electrostatic gate voltage tunes the chemical potential in the normal (N) region with respect to the potential in the superconducting (S) regions, thus, creating a potential

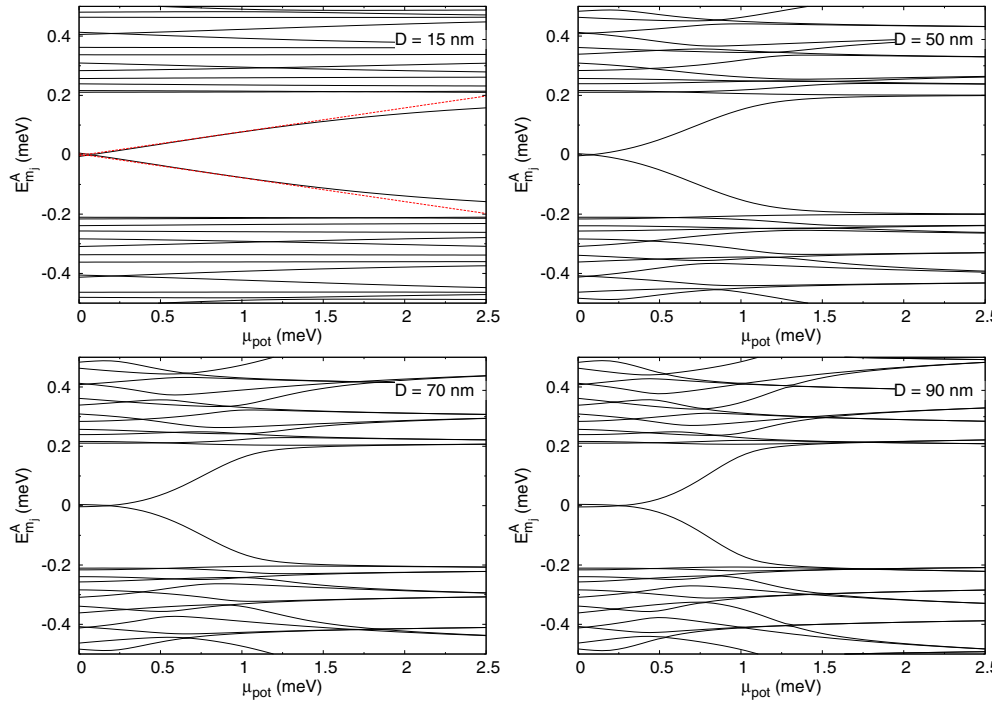

FIG. 5. Zero-flux energies of H_A [Eq. (3) main text] as a function of $\mu_{\rm pot}$ at phase difference $\varphi_0 = \pi$ for $m_j = 1/2$ and $K = \cosh$, with $E^A_{-m_j} = -E^B_{m_j}$ and $E^B_{m_j} = E^A_{m_j+1}$. Dashed curves for $D = 15$ nm are approximate energies derived from a two-level model described in the text. Parameters: $\mu_0 = 0.9$ meV, $L_S = 2000$ nm, $L_N = 100$ nm, $R_0 = 43$ nm, $\alpha = 0$, and $\Delta = \Delta_0 = 0.2$ meV.

offset between the N and S regions. The spatial profile of the chemical potential along the SNS junction is written as

$$\mu(z) = \mu_0 - \mu_{\rm pot} f(z), \tag{B1}$$

where the function $f(z)$ is expected to depend on the exact geometry of the junction, the microscopic details of the S-N interfaces, and the charge distribution in the junction. We consider a continuous variation across the S-N interfaces and assume that

$$f(z) = \frac{1}{K\left(\frac{(z-z_0)^2}{2D^2}\right)}, \tag{B2}$$

where for the function K we take either $K = \exp$ or $K = \cosh$, $z_0 = 0$ is the center of the N region, and $\mu_{\rm pot}$ ($\geqslant 0$) determines the potential offset. This offset is maximum in the center of the N region and the parameter D controls the length scale in which the chemical potential varies along the SNS junction. As shown below, for a large $\mu_{\rm pot}$ ($\approx \mu_0$) the critical current vanishes whereas it is maximum when $\mu_{\rm pot} \approx 0$. The results in the main text are for $\mu_{\rm pot} = 0$.

The effect of a nonzero $\mu_{\rm pot}$ on the energy spectra can be more easily understood in the regime of small μ_0, so that to a good approximation only the Hamiltonian H_A [Eq. (3) main text] is relevant with $m_j = 1/2$. One case illustrated in Fig. 5 demonstrates that increasing $\mu_{\rm pot}$ shifts the subgap levels (modes) near the edge of the superconducting gap. This shift in turn reduces the overall degree of φ_0-dispersion and consequently the critical current. Provided D and $\mu_{\rm pot}$ are small the term $-\mu_{\rm pot} f(z)$ can be treated within a perturbative two-level model, $H_A + \sigma_z \mu_{\rm pot} f(z)$, using for basis states the (two) subgap states at $\mu_{\rm pot} = 0$. Some results of this approximate model are presented in Fig. 5 for $D = 15$ nm; the agreement with the exact result is particularly good for small values of $\mu_{\rm pot}$ and the correct linear behavior is predicted. The two-level model can also predict the correct φ_0 dispersion, however, by increasing D the model becomes quickly inaccurate. For example, when $D = 50$ nm and $\mu_{\rm pot} \approx 1$ meV, about 60 basis states are needed to achieve the same convergence as for $D = 15$ nm.

A more general configuration is now examined when the energy levels lying in the superconducting gap correspond to different m_j values. Some typical energy spectra of H_A are plotted in Fig. 6. At $\mu_{\rm pot} = 0$ the subgap levels correspond to $m_j = 1/2$, $3/2$, and $5/2$, thus, there are five positive levels: $E^A_{1/2}$, $E^B_{1/2}$, $E^A_{3/2}$, $E^B_{3/2}$, and $E^A_{5/2}$ with the degeneracies $E^B_{1/2} = E^A_{3/2}$ as well as $E^B_{3/2} = E^A_{5/2}$. As shown in Fig. 6, increasing $\mu_{\rm pot}$ tends to shift the subgap levels outside (near the edge of) the gap in a systematic way. In particular, levels which correspond to larger m_j shift outside the gap at smaller values of $\mu_{\rm pot}$, and consequently, the number of active modes in the SNS junction can be controlled at will.

When the energy levels shift outside the gap the critical current decreases and eventually complete suppression occurs when $\mu_{\rm pot} \approx \mu_0$ (Fig. 7). The exact form of $f(z)$ determines the details of the overall process. Specifically, the decrease of the current is not necessarily monotonic and current steps can be formed because the different m_j levels are not affected equally by the potential term $\mu_{\rm pot}$.

APPENDIX C: SIMPLIFIED SNS JUNCTION MODEL

In this section, we present in some detail the simplified SNS junction model introduced in the main text. The subgap

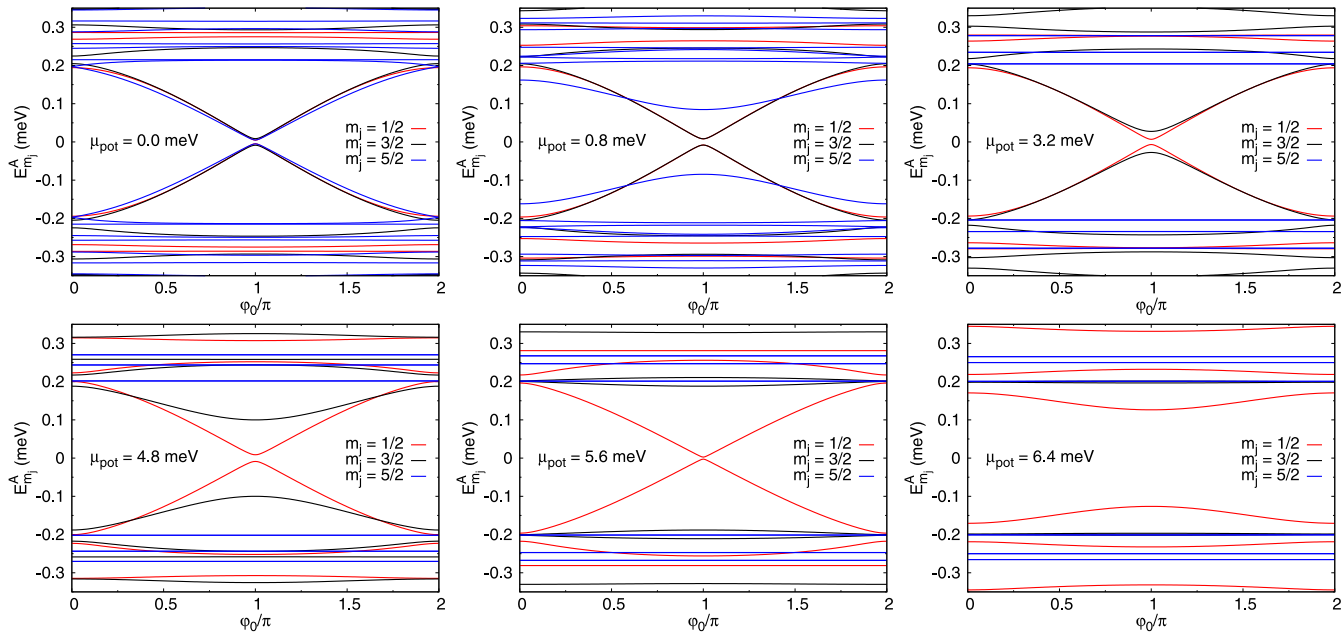

FIG. 6. Zero-flux energies of H_A [Eq. (3) main text] as a function of phase difference φ_0 for $K = \cosh$, with $E^A_{-m_j} = -E^B_{m_j}$ and $E^B_{m_j} = E^A_{m_j+1}$. Parameters: $D = 70$ nm, $\mu_0 = 6.5$ meV, $L_S = 2000$ nm, $L_N = 100$ nm, $R_0 = 43$ nm, $\alpha = 0$, and $\Delta = \Delta_0 = 0.2$ meV.

modes are written as follows ($\hbar = 1$)

$$E_{\pm,k}(\varphi_0, \Phi) = \pm\Delta\sqrt{1 - \tau_k \sin^2(\varphi_0/2)} + w_k \frac{\Phi}{\Phi_0}, \qquad \text{(C1)}$$

with $k = 1, 2, \ldots, M$,

$$w_k = \frac{(k-1)}{2m^* R_0^2}, \qquad \text{(C2)}$$

and $\Delta = \Delta(\Phi)$ everywhere. To avoid confusion we note a few remarks. Firstly, we focus on $w_k \geqslant 0$ and multiply the currents by 2 to account for $\pm m_j$. Secondly, the term $w_k\Phi/\Phi_0$ results in the same flux dependence as $\delta^+_{m_j}$ in the main text [Eq. (6)] for the zeroth lobe, $n = 0$, and zero SO coupling, $\alpha = 0$. The first lobe, $n = 1$, can be treated similarly. Finally, the degeneracy due to $H_B(m_j) = H_A(m_j + 1)$ is not considered in Eq. (C1) since this does not change qualitatively the final conclusions.

When all w_k are zero and $\tau_k = \tau$ the supercurrent is written as $MI_Z(\varphi_0)$ with

$$I_Z(\varphi_0) = -\frac{e}{\hbar}\frac{\Delta}{2}\frac{\tau \sin\varphi_0}{\sqrt{1 - \tau \sin^2(\varphi_0/2)}}, \qquad \text{(C3)}$$

while the phase $\tilde{\varphi}_0$ ($\leqslant \pi$) giving the critical current, I^c, can be readily extracted. An interesting remark is that when $w_k \neq 0$ the critical current can be expressed with the help of the supercurrent I_Z. Specifically, for $k \neq 1$ we define within the flux range $\Delta\sqrt{1-\tau} < w_k\Phi/\Phi_0 \leqslant \Delta$ the corresponding flux-dependent phase $\theta_k = \theta_k(\Phi)$ satisfying $E_{-,k}(\theta_k) = 0$,

$$\theta_k = 2\sin^{-1}\sqrt{\frac{1}{\tau}\left(1 - \frac{w_k^2\Phi^2}{\Delta^2\Phi_0^2}\right)}, \qquad \text{(C4)}$$

with $0 \leqslant \theta_k \leqslant \pi$. As Φ increases, I^c follows the $\Delta(\Phi)$ dependence until $\theta_M = \tilde{\varphi}_0$, but when $\theta_M < \tilde{\varphi}_0$ the decrease of I^c due

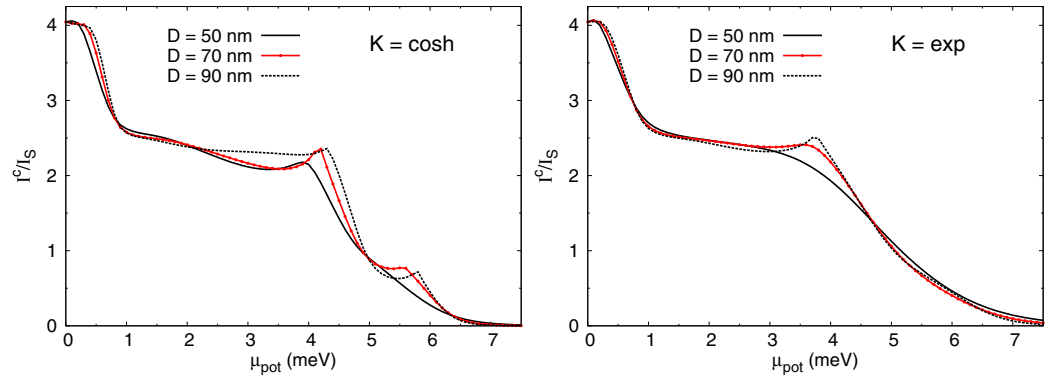

FIG. 7. Zero-flux critical current as a function of $\mu_{\rm pot}$. Parameters: $\mu_0 = 6.5$ meV, $L_S = 2000$ nm, $L_N = 100$ nm, $R_0 = 43$ nm, $\alpha = 0$, $\Delta = \Delta_0 = 0.2$ meV, and $I_S = e\Delta_0/\hbar$.

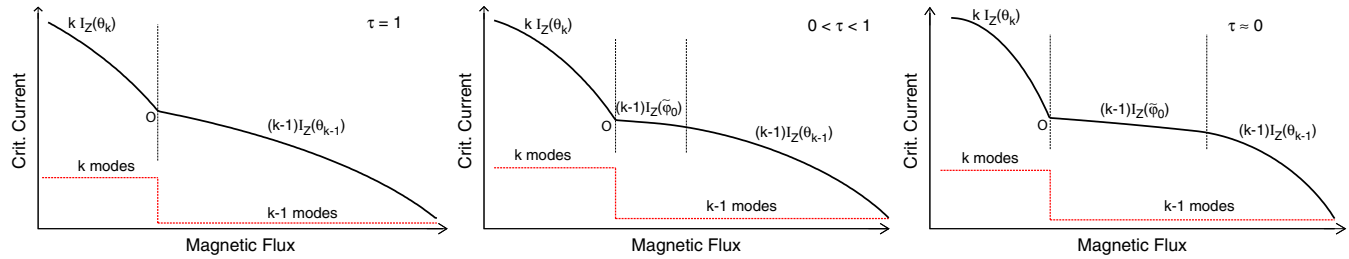

FIG. 8. Illustration of flux tunable critical current and number of subgap modes predicted by simplified model, Eq. (C1). A single kink point (O) is indicated in each frame. A detailed explanation is given in the text.

to w_k needs to be accounted for. Now I^c is equal to the largest of the three terms $kI_Z(\theta_k)$, $(k-1)I_Z(\tilde{\varphi}_0)$ and $(k-1)I_Z(\theta_{k-1})$; and as Φ increases $k \to k-1$, hence, the number of subgap modes contributing to the current decreases successively by one. This process gives rise to a stepwise current profile and is illustrated in Fig. 8. For $\tau \to 1$ ($\tilde{\varphi}_0 \to \pi$), the flux range where $(k-1)I_Z(\tilde{\varphi}_0)$ needs to be considered vanishes/shrinks, and only the two terms $kI_Z(\theta_k)$, $(k-1)I_Z(\theta_{k-1})$ are important. When $kI_Z(\theta_k) = (k-1)I_Z(\theta_{k-1})$ a kink point is formed, and using Eq. (C4) with

$$I_Z(\varphi_0) = -\frac{e}{\hbar}\Delta \sin(\varphi_0/2), \tag{C5}$$

we can determine the corresponding flux value

$$\frac{\Phi}{\Phi_0} = \Delta(\Phi)\sqrt{\frac{k^2-(k-1)^2}{k^2 w_k^2 - (k-1)^2 w_{k-1}^2}}. \tag{C6}$$

In the opposite limit, $\tau \to 0$ ($\tilde{\varphi}_0 \to \pi/2$), the flux range where $(k-1)I_Z(\tilde{\varphi}_0)$ dominates is maximum and current steps are clearly formed. A kink point is now formed when $kI_Z(\theta_k) = (k-1)I_Z(\tilde{\varphi}_0)$, which is satisfied for

$$\frac{\Phi}{\Phi_0} \approx \frac{\Delta(\Phi)}{w_k}, \tag{C7}$$

considering that $I_Z(\varphi_0) \approx -e\Delta\tau \sin(\varphi_0)/\hbar$. The current steps become flatter as the flux dependence of $(k-1)I_Z(\tilde{\varphi}_0)$, due to $\Delta(\Phi)$, weakens. In this analysis, because of the special value $w_1 = 0$ we have $I_Z(\theta_1) \to I_Z(\tilde{\varphi}_0)$ for any value of τ. The $k = 1$ mode does not shift with flux and the number of subgap modes drops to zero at the boundaries of the lobe because $\Delta(\Phi) = 0$.

In Fig. 9, we plot the critical current for different number of subgap modes M. By increasing M, extra steps/kink points are formed. Most importantly, the overall current profile is qualitatively the same as that derived from the exact BdG Hamiltonian; see for example Fig. 4 for $n = 0$ in the main text. For $M = 1$ and because $w_1 = 0$, the current can be described by the formula $I^c(\Phi) = I^c(0)\Delta(\Phi)/\Delta_0$, in stark contrast for $M > 1$ this formula is inapplicable.

In Fig. 10, we take $M = 4$ and plot typical examples of the critical current for three different radii R_0. For a better comparison, we adjust the coherence length of the shell ξ so that for each R_0 the pairing potential vanishes when $|\Phi/\Phi_0| \gtrsim 0.45$. For illustrative reasons, we also present one case for an unrealistically large radius, $R_0 = 160$ nm. The purpose is to demonstrate how the size of w_k affects the overall profile of the current. The role of the terms w_k weakens for larger values of R_0. In particular, when the ratio $1/m^* R_0^2$ becomes vanishingly small the required magnetic flux to induce a kink point lies nearly at the boundaries of the lobe. In the regime, $w_k \approx 0$, the flux dependence of the current can be accurately described by the formula $I^c(\Phi) = I^c(0)\Delta(\Phi)/\Delta_0$; when $\tau = 1$ this equals $Me\Delta(\Phi)/\hbar$. Another important observation is that for smaller values of w_k the flux dependence of θ_k is weaker. This explains why for a given radius R_0 the current steps which are formed at larger fluxes are in general broader (Fig. 10).

So far in our analysis we have focused on $\tau_k = \tau$, but our results can be easily generalized to the most general case when the transparency, τ_k, of each individual mode is different. Some analytical expressions for the critical current can again be derived, however, these are not particularly enlightening. The important conclusion is that all the basic features presented in Figs. 9 and 10 are still observable in the most general case. Our analysis is also applicable when the φ_0-dispersion of the subgap modes is different from that specified by

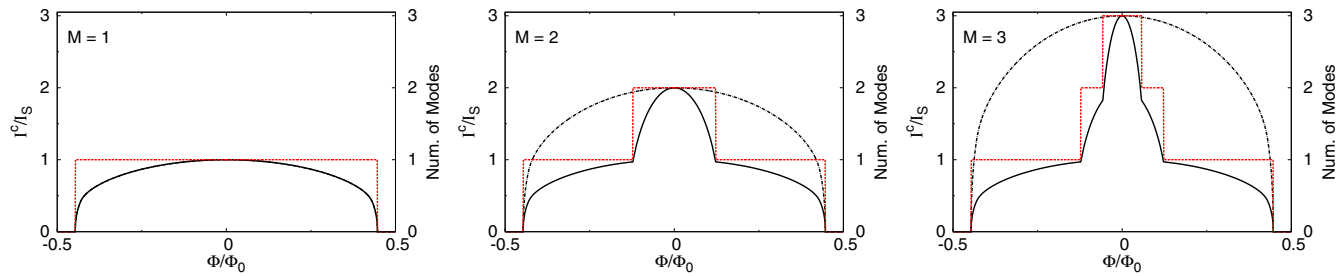

FIG. 9. Critical current and number of subgap modes (dotted lines, right axis) derived from simplified model, Eq. (C1), with $\tau_k = \tau = 1$, $R_0 = 43$ nm, and $I_S = e\Delta_0/\hbar$. Dash-dotted curves show $I^c(0)\Delta/\Delta_0$; this coincides with the critical current for $M = 1$. Δ is calculated from Eq. (A1) with $\xi = 80$ nm, $d_{sc} = 0$, and $\Delta_0 = 0.2$ meV.

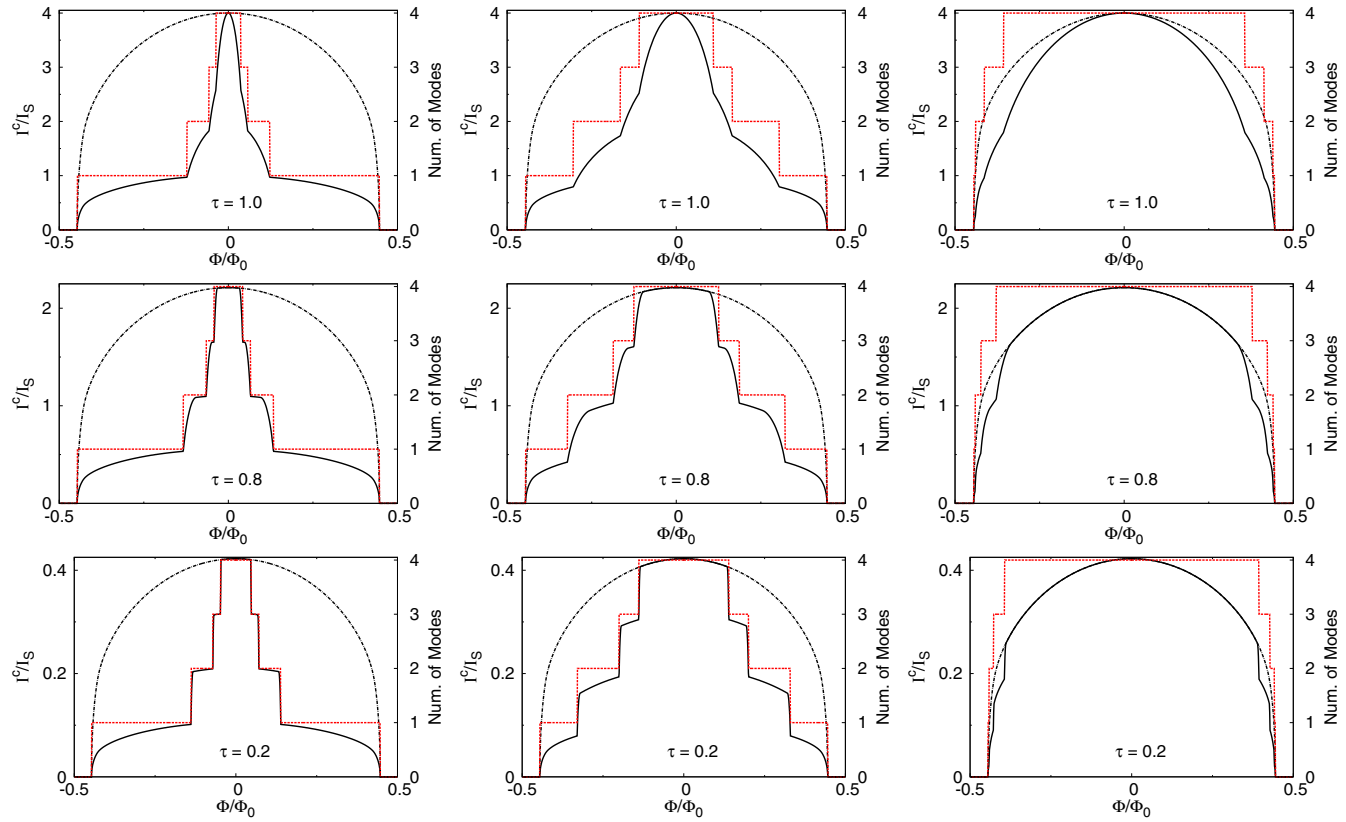

FIG. 10. Critical current and number of subgap modes (dotted lines, right axis) derived from simplified model, Eq. (C1), with $M = 4$, $\tau_k = \tau$, and $I_S = e\Delta_0/\hbar$. Dash-dotted curves show $I^c(0)\Delta/\Delta_0$. First column: $R_0 = 43$ nm, $\xi = 80$ nm. Second column: $R_0 = 75$ nm, $\xi = 140$ nm. Third column: $R_0 = 160$ nm, $\xi = 299$ nm. Δ is calculated from Eq. (A1) with $d_{sc} = 0$, $\Delta_0 = 0.2$ meV.

Eq. (C1). Numerically calculated subgap modes derived from the exact BdG Hamiltonian can equally well demonstrate the physics.

The stepwise current profile is independent of the number of subgap modes. Both Eqs. (9) and (10) in the main text, are independent of the number of subgap modes and they are valid even if we assume an infinite number of modes. By adding extra modes the current acquires a sharper flux dependence, near the lobe center, due to the larger m_j values involved in the dynamics. To quantify these arguments we present in Fig. 11 examples with $M = 5$, 10, and 20 modes. The basic conclusions are: (i) the current steps near the lobe center are sharper compared to the steps at larger fluxes, and (ii) the overall current profile as a function of the magnetic flux is completely different from the Little-Parks modulation of the pairing potential.

Finally, we mention that our results are not limited to zero temperature, $T = 0$ K. However, as with any mesoscopic system, an increase in temperature tends to wash out the current steps. We perform finite-temperature calculations using the supercurrent-phase formula

$$I(\varphi_0) = -\frac{e}{\hbar}\sum_{E>0}\tanh\left(\frac{E}{2k_BT}\right)\frac{dE}{d\varphi_0}, \tag{C8}$$

where in the context of the simplified model $E \equiv E_{\pm,k}(\varphi_0, \Phi)$ and k_B is Boltzman's constant. In Fig. 12, we show a few examples of how the temperature affects the critical current. For

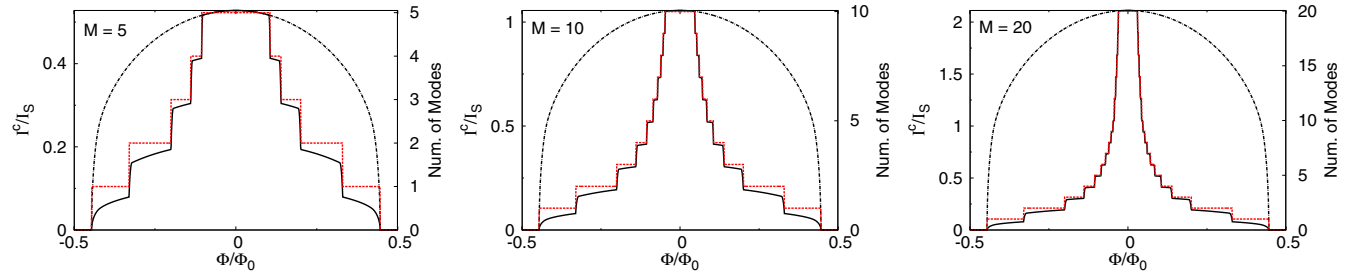

FIG. 11. Critical current and number of subgap modes (dotted lines, right axis) derived from simplified model, Eq. (C1), with $\tau_k = \tau = 0.2$, $R_0 = 75$ nm, and $I_S = e\Delta_0/\hbar$. Dash-dotted curves show $I^c(0)\Delta/\Delta_0$. Δ is calculated from Eq. (A1) with $\xi = 140$ nm, $d_{sc} = 0$, and $\Delta_0 = 0.2$ meV.

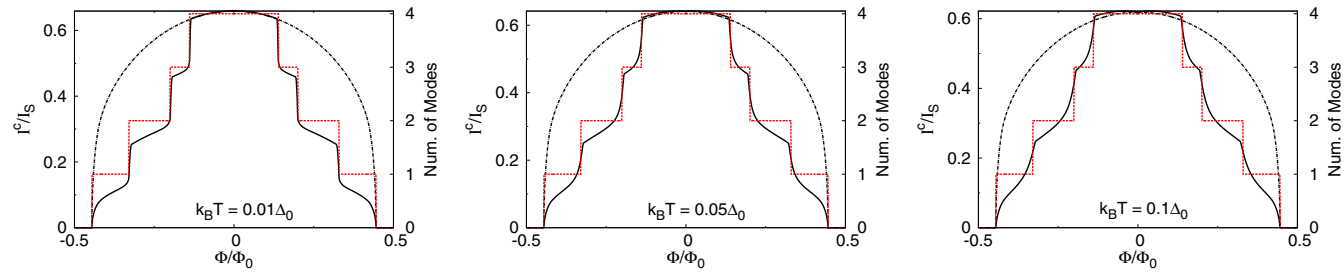

FIG. 12. Critical current and number of subgap modes (dotted lines, right axis) derived from simplified model, Eq. (C1), at different temperatures, with $M = 4$, $\tau_k = \tau = 0.2$, $R_0 = 75$ nm, and $I_S = e\Delta_0/\hbar$. Dash-dotted curves show $I^c(0)\Delta/\Delta_0$. Δ is calculated from Eq. (A1) with $\xi = 140$ nm, $d_{sc} = 0$, and $\Delta_0 = 0.2$ meV.

clarity we consider Δ_0 to be temperature independent. When the temperature is of the order of $k_BT \approx 0.1\Delta_0$ ($T \approx 0.2$ K) or lower the stepwise behavior can be nicely observed. The effect of the temperature is weaker in SNS junctions with smaller transparencies because in these junctions the current steps are in general sharper.

APPENDIX D: FLUX TUNABLE CURRENT IN A REDUCED TRANSPARENCY JUNCTION

In the main text, we consider an ideal SNS junction, namely, a transparent junction where there is no explicit physical mechanism to suppress tunneling between the S and N regions. As introduced above, a spatially dependent chemical potential controls the number of subgap levels as well as the current, but this control is sensitive to the value of m_j. In this respect, it is interesting to explore how the degree of transparency affects the current when the number of subgap levels remains approximately constant. This can be done using again Eq. (B1), but now the parameter D needs to be carefully optimized. This makes the computational procedure inefficient and time consuming. For this reason, we model the transparency of the junction phenomenologically by employing a similar methodology to that presented originally in Ref. [58]. Specifically, in the BdG Hamiltonian we introduce a dimensionless parameter τ_0, with $0 < \tau_0 \leqslant 1$, which scales the kinetic terms along the z direction ($\tau_0 p_z^2/2m^*$). We assume this scaling to take place within the N region and an adjacent small part ($x_S \approx 20$ nm $\ll L_S$) in the S regions. The transparent limit (main text) corresponds to $\tau_0 = 1$, whereas the opposite limit, $\tau_0 \approx 0$, is not of interest here since the critical current is almost completely suppressed. Thus, in this work,

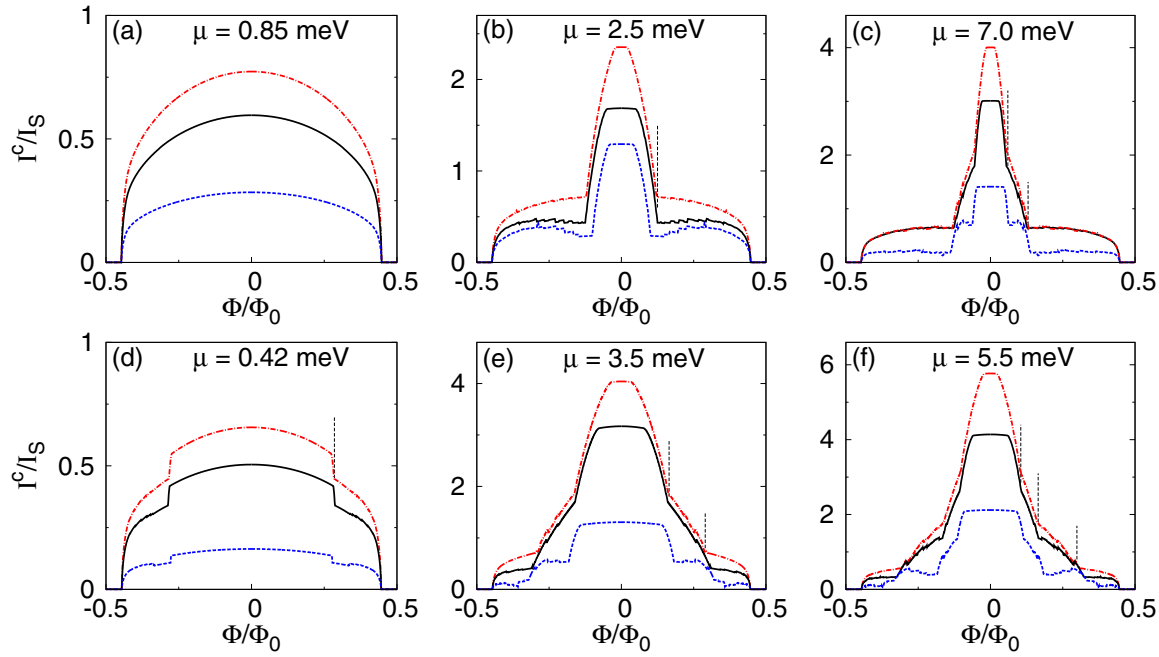

FIG. 13. Critical current as a function of magnetic flux calculated with Δ given by Eq. (A1). From upper to lower curve: $\tau_0 = 1$, 0.6, and 0.2. Parameters: $L_S = 2000$ nm, $L_N = 100$ nm, $\alpha = 0$, $\Delta_0 = 0.2$ meV, $d_{sc} = 0$, and $I_S = e\Delta_0/\hbar$. [(a)–(c)] $R_0 = 43$ nm, $\xi = 80$ nm. [(d)–(f)] $R_0 = 75$ nm, $\xi = 140$ nm. Vertical lines indicate kink points for $\tau_0 = 1$. As Φ increases the number of nondegenerate subgap modes decreases by one at each kink point. The latter, in general, shift for different τ_0. At $\Phi = 0$, the subgap modes contributing to the current are derived from: (a) $m_j = 1/2$; (b) $m_j = 1/2$ and $3/2$; (c) $m_j = 1/2$, $3/2$, and $5/2$; (d) $m_j = 1/2$ and $3/2$; (e) $m_j = 1/2$, $3/2$, and $5/2$; and (f) $m_j = 1/2$, $3/2$, $5/2$, and $7/2$.

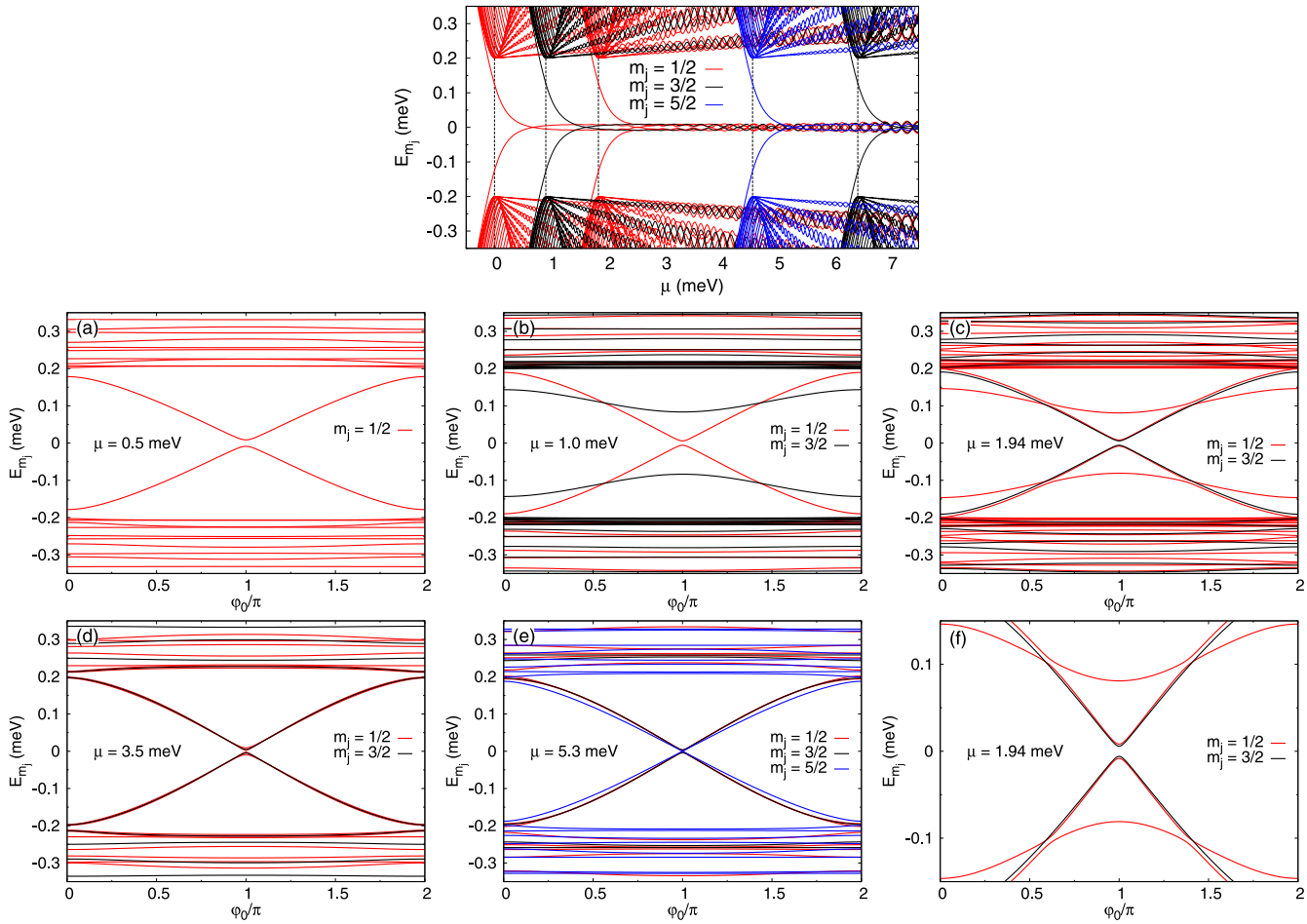

FIG. 14. (Top) Zero-flux energy spectrum of SNS junction as a function of chemical potential at phase difference $\varphi_0 = \pi$. Energies are derived from H_{BdG} [Eq. (2) main text] and satisfy $E_{-m_j} = -E_{mj}$. Vertical lines define the effective potentials $V_1^0(m_j) \approx 0$ and $V_3^0(m_j) \approx 0$ for $m_j = 1/2$, $3/2$, and $5/2$. [(a)–(e)] Energies as a function of phase difference at different chemical potentials. Only energies lying within the chosen energy range are plotted. (f) Zoom in of (c) showing anticrossing point for $m_j = 1/2$ due to the SO coupling. Parameters: $L_S = 2000$ nm, $L_N = 100$ nm, $R_0 = 43$ nm, $\alpha = 20$ meV nm, and $\Delta = \Delta_0 = 0.2$ meV.

we choose the lower limit to be $\tau_0 = 0.2$ which allows us to capture all the essential characteristics.

For the computations, the kinetic term along the z direction is written as ($\hbar = 1$)

$$T_{\mathrm{kin}} = -\frac{1}{2m^*}\frac{d}{dz}\left(\tau_0(z)\frac{dy(z)}{dz}\right), \tag{D1}$$

where $y(z)$ represents any of the four components of the BdG Hamiltonian. Using centered differences and defining τ_0 on the mid lattice points the kinetic term is discretized as follows:

$$T_{\mathrm{kin}} \approx b^{i-1}y^{i-1} - [b^{i-1} + b^i]y^i + b^i y^{i+1}, \tag{D2}$$

with

$$b^i = -\frac{1}{2m^*\delta^2}\tau_0^{i+1/2}, \quad b^{i-1} = -\frac{1}{2m^*\delta^2}\tau_0^{i-1/2}, \tag{D3}$$

and δ is the spacing between the lattice points. Here, b^i describes hopping between the lattice points i and $i+1$ while $\tau_0^{i+1/2}$ is the value of the transparency between these two lattice points. When τ_0 is constant the usual finite-difference approximation to the kinetic term is recovered.

We calculate the critical current using the approximation described in the main text and show some representative numerical results in Fig. 13. Note that as happens with the current suppression versus μ_{pot} in Fig. 7, the current suppression versus τ_0 at a fixed chemical potential and flux is not always monotonic. As τ_0 decreases the basic flux tunable features are well-formed at least for intermediate ($\tau_0 \approx 0.5$) and somewhat smaller values of τ_0. Our calculations within the exact BdG Hamiltonian confirm that this behavior is robust for different sets of parameters: R_0, μ, and x_S. They also indicate that the form of the current steps does not necessarily improve upon decreasing τ_0. Although, some steps become more pronounced this cannot be guaranteed to be the general rule. In our SNS junction with energy levels above the gap contributing to the current and with an explicit μ (and/or μ_{pot}) dependence, the underlying physics is expected to deviate to some degree from that derived from the simplified model. Energy levels which lie above the gap at $\Phi = 0$ tend to make the steps more "noisy" at $\Phi \neq 0$, and the overall noise is sensitive to the exact values of μ and τ_0. These effects are not captured by the simplified model. The quality of the steps is expected to improve in SNS junctions with a shorter N region. Another

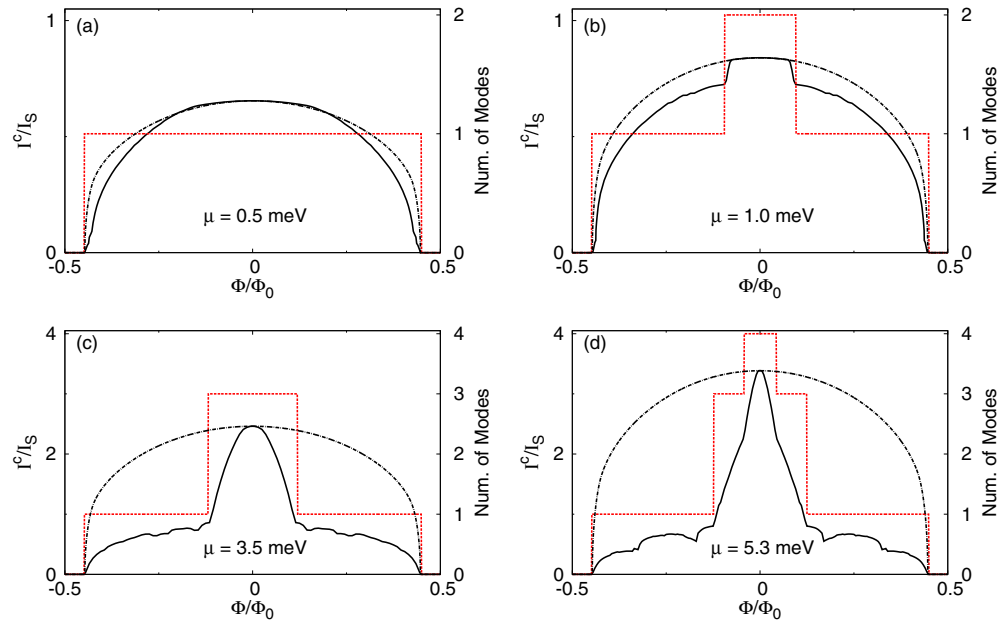

FIG. 15. Solid curves show the exact critical current, $I^c(\Phi)$, calculated with Δ given by Eq. (A1). Dash-dotted curves show $I^c(0)\Delta/\Delta_0$. Dotted lines show the number of subgap modes (right axis). Parameters: $L_S = 2000$ nm, $L_N = 100$ nm, $R_0 = 43$ nm, $\alpha = 20$ meV nm, $\Delta_0 = 0.2$ meV, $\xi = 80$ nm, $d_{sc} = 0$, and $I_S = e\Delta_0/\hbar$. At $\Phi = 0$ the subgap modes contributing to the current are derived from: (a) $m_j = 1/2$; (b) $m_j = 1/2$ and $3/2$; (c) $m_j = 1/2$ and $3/2$; and (d) $m_j = 1/2$, $3/2$, and $5/2$.

important aspect, which might be relevant to experimental studies, is that the current steps which are formed at larger fluxes can be almost completely suppressed for a relatively small τ_0. This effect can lead to the wrong conclusion that the current suppression is due to the LP effect. A rigorous method to disentangle the LP-induced current suppression from that caused by τ_0 deserves further investigation.

APPENDIX E: SNS JUNCTION WITH SPIN-ORBIT COUPLING

In this section, we examine the effect of the Rashba spin-orbit (SO) coupling on the flux dependence of the critical current. Our aim is to demonstrate that the current profile presented in Fig. 4 of the main text can still be observed in the presence of a weak SO coupling. Analyzing in detail SO effects is beyond the scope of this work.

We consider the chemical potential, μ, to be constant along the SNS junction, thus, as explained above we focus on the resonant case where the critical current is maximum. A nonuniform μ simply results in a reduced current. A nonzero SO coupling, α, shifts further apart the values of μ at which the energy levels of $H_A(m_j)$ and $H_B(m_j)$ respectively enter the superconducting gap. This shift is of the order of $2m_j\alpha/R_0$ as can be understood directly from Eqs. (4) in the main text. In addition, when $\alpha \neq 0$ the energies of $H_A(m_j + 1)$ and $H_B(m_j)$ are no longer degenerate, since $V_1^0(m_j + 1) \neq V_3^0(m_j)$, and when the parameters are tuned so that ($\hbar = 1$)

$$\alpha \approx \frac{2m_j - 1}{4m^* R_0}, \tag{E1}$$

the condition $V_1^0(m_j) \approx -\mu$ can be satisfied for $m_j > 1/2$ (assuming $\Phi = 0$). In this regime and at low chemical potentials, the critical current is no longer dominated by $m_j = 1/2$ only, therefore, an enhanced critical current can be observed compared to that for $\alpha = 0$. A subtle point is that this enhancement is not due to the actual coupling between $H_A(m_j)$ and $H_B(m_j)$ caused by $H_{SO}^z = -\alpha\partial_z\tilde{\tau}_z$, but to the rearrangement of the potentials terms $V_1^0(m_j)$ and $V_3^0(m_j)$.

For the numerical calculations, we consider a realistic value for the SO coupling in the relatively weak regime, $\alpha = 20$ meV nm, and assume that α is constant along the SNS junction. This can be considered as a first approximation, since α may have a spatial dependence and/or be anisotropic, for example, due to local electric fields induced by gate electrodes. Additionally the sign of α is in general unknown. All these effects should depend on the details of the SNS junction, however, small deviations from a constant SO coupling are not expected to change the flux dependence of the critical current studied here. Our numerical calculations confirm this argument when α is assumed to be different in the N and S regions.

The zero-flux energies of the BdG Hamiltonian [Eq. (2) main text] are plotted in Fig. 14. For each m_j we can identify the approximate value of μ that shifts an energy level, originally belonging to $H_A(m_j)$ or $H_B(m_j)$, in the superconducting gap by setting $V_1^0(m_j) \approx 0$ or $V_3^0(m_j) \approx 0$ respectively. The energies as a function of the superconducting phase exhibit similar overall characteristics to $\alpha = 0$. However, an important difference is the formation of anticrossing points between the energy levels of $H_A(m_j)$ and $H_B(m_j)$ [Figs. 14(c) and 14(f)] as a result of the SO Hamiltonian $H_{SO}^z = -\alpha\partial_z\tilde{\tau}_z$. The anticrossing point is formed at a phase (in general $\varphi_0 \neq \pi$) which is sensitive to the chemical potential and the same sensitivity is observed for the corresponding value of the anticrossing gap.

In Fig. 15, we present the critical current, derived from the BdG Hamiltonian, as a function of the magnetic flux for

various chemical potentials. The basic characteristics are the same as in Fig. 4 in the main text for $\alpha = 0$. At a small potential ($\mu = 0.5$ meV), and to a very good approximation, only $m_j = 1/2$ is relevant contributing a single subgap mode, and the usual formula $I^c(0)\Delta/\Delta_0$ is in good agreement with the exact current. In contrast, this formula is no longer valid for large values of μ when extra subgap modes contribute to the current. The SO coupling modifies the flux dependence of the effective potentials, $\delta^{\pm}_{m_j}$, [Eq. (6) main text] by introducing an additional shift $\pm\alpha/2R_0$; for $\alpha = 20$ meV nm, this shift is small especially for larger m_j modes. Therefore, within a simplified approach, a finite flux shifts the $\Phi = 0$ subgap modes outside the superconducting gap in a similar way to the $\alpha = 0$ case. An exception occurs for the subgap mode belonging to $H_A(m_j = 1/2)$, for which $\delta^{+}_{1/2} \neq 0$ provided $\alpha \neq 0$, but, numerical calculations in the range of parameters considered here do not indicate any significant difference in the current from that when $\alpha = 0$. The regime where only $H_A(m_j = 1/2)$ is relevant is the simplest one to probe the SO coupling; large values of α should induce a kink point well within the lobe and the resulting flux dependence of I^c should deviate to some degree from that of Δ. For the proper μ and α, when both H_A and H_B are relevant, the SO-induced anticrossings are expected to add some new features to the flux dependence of the current. Rather small dips can already be seen in Fig. 15(d) in the single mode regime, however, this investigation is not pursued in this work.

[1] Y.-J. Doh, J. A. van Dam, A. L. Roest, E. P. A. M. Bakkers, L. P. Kouwenhoven, and S. De Franceschi, Science **309**, 272 (2005).

[2] M. T. Deng, C. L. Yu, G. Y. Huang, M. Larsson, P. Caroff, and H. Q. Xu, Nano Lett. **12**, 6414 (2012).

[3] K. Gharavi, G. W. Holloway, C. M. Haapamaki, M. H. Ansari, M. Muhammad, R. R. LaPierre, and J. Baugh, arXiv:1405.7455.

[4] K. Zuo, V. Mourik, D. B. Szombati, B. Nijholt, D. J. van Woerkom, A. Geresdi, J. Chen, V. P. Ostroukh, A. R. Akhmerov, S. R. Plissard *et al.*, Phys. Rev. Lett. **119**, 187704 (2017).

[5] P. Sriram, S. S. Kalantre, K. Gharavi, J. Baugh, and B. Muralidharan, Phys. Rev. B **100**, 155431 (2019).

[6] J. Tiira, E. Strambini, M. Amado, S. Roddaro, P. San-Jose, R. Aguado, F. S. Bergeret, D. Ercolani, L. Sorba, and F. Giazotto, Nat. Commun. **8**, 14984 (2017).

[7] S. Hart, Z. Cui, G. Ménard, M. Deng, A. E. Antipov, R. M. Lutchyn, P. Krogstrup, C. M. Marcus, and K. A. Moler, Phys. Rev. B **100**, 064523 (2019).

[8] D. J. Carrad, M. Bjergfelt, T. Kanne, M. Aagesen, F. Krizek, E. M. Fiordaliso, E. Johnson, J. Nygård, and T. S. Jespersen, Adv. Mater. **32**, 1908411 (2020).

[9] S. A. Khan, C. Lampadaris, A. Cui, L. Stampfer, Y. Liu, S. J. Pauka, M. E. Cachaza, E. M. Fiordaliso, J.-H. Kang, S. Korneychuk *et al.*, ACS Nano **14**, 14605 (2020).

[10] J. A. Sauls, Philos. Trans. R. Soc. A **376**, 20180140 (2018).

[11] L. Tosi, C. Metzger, M. F. Goffman, C. Urbina, H. Pothier, S. Park, A. L. Yeyati, J. Nygård, and P. Krogstrup, Phys. Rev. X **9**, 011010 (2019).

[12] J. Cayao, E. Prada, P. San-Jose, and R. Aguado, Phys. Rev. B **91**, 024514 (2015).

[13] A. Bargerbos, M. Pita-Vidal, R. Žitko, L. J. Splitthoff, L. Grünhaupt, J. J. Wesdorp, Y. Liu, L. P. Kouwenhoven, R. Aguado, C. K. Andersen *et al.*, Phys. Rev. Lett. **131**, 097001 (2023).

[14] F. J. Matute-Cañadas, C. Metzger, S. Park, L. Tosi, P. Krogstrup, J. Nygård, M. F. Goffman, C. Urbina, H. Pothier, and A. L. Yeyati, Phys. Rev. Lett. **128**, 197702 (2022).

[15] A. Bargerbos, M. Pita-Vidal, R. Žitko, J. Ávila, L. J. Splitthoff, L. Grünhaupt, J. J. Wesdorp, C. K. Andersen, Y. Liu, L. P. Kouwenhoven *et al.*, PRX Quantum **3**, 030311 (2022).

[16] V. Fatemi, P. D. Kurilovich, M. Hays, D. Bouman, T. Connolly, S. Diamond, N. E. Frattini, V. D. Kurilovich, P. Krogstrup, J. Nygård *et al.*, Phys. Rev. Lett. **129**, 227701 (2022).

[17] V. Chidambaram, A. Kringhøj, L. Casparis, F. Kuemmeth, T. Wang, C. Thomas, S. Gronin, G. C. Gardner, Z. Cui, C. Liu *et al.*, Phys. Rev. Res. **4**, 023170 (2022).

[18] R. Aguado, Appl. Phys. Lett. **117**, 240501 (2020).

[19] T. W. Larsen, K. D. Petersson, F. Kuemmeth, T. S. Jespersen, P. Krogstrup, J. Nygård, and C. M. Marcus, Phys. Rev. Lett. **115**, 127001 (2015).

[20] G. de Lange, B. van Heck, A. Bruno, D. J. van Woerkom, A. Geresdi, S. R. Plissard, E. P. A. M. Bakkers, A. R. Akhmerov, and L. DiCarlo, Phys. Rev. Lett. **115**, 127002 (2015).

[21] L. Casparis, T. W. Larsen, M. S. Olsen, F. Kuemmeth, P. Krogstrup, J. Nygård, K. D. Petersson, and C. M. Marcus, Phys. Rev. Lett. **116**, 150505 (2016).

[22] A. Kringhøj, G. W. Winkler, T. W. Larsen, D. Sabonis, O. Erlandsson, P. Krogstrup, B. van Heck, K. D. Petersson, and C. M. Marcus, Phys. Rev. Lett. **126**, 047701 (2021).

[23] D. Sabonis, O. Erlandsson, A. Kringhøj, B. van Heck, T. W. Larsen, I. Petkovic, P. Krogstrup, K. D. Petersson, and C. M. Marcus, Phys. Rev. Lett. **125**, 156804 (2020).

[24] M. Hays, V. Fatemi, D. Bouman, J. Cerrillo, S. Diamond, K. Serniak, T. Connolly, P. Krogstrup, J. Nygård, A. L. Yeyati *et al.*, Science **373**, 430 (2021).

[25] M. Pita-Vidal, A. Bargerbos, R. Žitko, L. J. Splitthoff, L. Grünhaupt, J. J. Wesdorp, Y. Liu, L. P. Kouwenhoven, R. Aguado, B. van Heck *et al.*, Nature Physics **19**, 1110 (2023).

[26] T. W. Larsen, M. E. Gershenson, L. Casparis, A. Kringhøj, N. J. Pearson, R. P. G. McNeil, F. Kuemmeth, P. Krogstrup, K. D. Petersson, and C. M. Marcus, Phys. Rev. Lett. **125**, 056801 (2020).

[27] C. Schrade, C. M. Marcus, and A. Gyenis, PRX Quantum **3**, 030303 (2022).

[28] D. Aasen, M. Hell, R. V. Mishmash, A. Higginbotham, J. Danon, M. Leijnse, T. S. Jespersen, J. A. Folk, C. M. Marcus, K. Flensberg *et al.*, Phys. Rev. X **6**, 031016 (2016).

[29] T. Karzig, C. Knapp, R. M. Lutchyn, P. Bonderson, M. B. Hastings, C. Nayak, J. Alicea, K. Flensberg, S. Plugge, Y. Oreg *et al.*, Phys. Rev. B **95**, 235305 (2017).

[30] R. Aguado and L. P. Kouwenhoven, Phys. Today **73**(6), 44 (2020).

[31] P. Krogstrup, N. L. B. Ziino, W. Chang, S. M. Albrecht, M. H. Madsen, E. Johnson, J. Nygård, C. M. Marcus, and T. S. Jespersen, Nat. Mater. **14**, 400 (2015).

[32] S. Vaitiekenas, G. W. Winkler, B. van Heck, T. Karzig, M.-T. Deng, K. Flensberg, L. I. Glazman, C. Nayak, P. Krogstrup, R. M. Lutchyn *et al.*, Science **367**, eaav3392 (2020).
[33] F. Peñaranda, R. Aguado, P. San-Jose, and E. Prada, Phys. Rev. Res. **2**, 023171 (2020).
[34] M. Valentini, F. Peñaranda, A. Hofmann, M. Brauns, R. Hauschild, P. Krogstrup, P. San-Jose, E. Prada, R. Aguado, and G. Katsaros, Science **373**, 82 (2021).
[35] M. Valentini, M. Borovkov, E. Prada, S. Martí-Sánchez, M. Botifoll, A. Hofmann, J. Arbiol, R. Aguado, P. San-Jose, and G. Katsaros, Nature (London) **612**, 442 (2022).
[36] S. Vaitiekėnas, P. Krogstrup, and C. M. Marcus, Phys. Rev. B **101**, 060507(R) (2020).
[37] W. A. Little and R. D. Parks, Phys. Rev. Lett. **9**, 9 (1962).
[38] R. D. Parks and W. A. Little, Phys. Rev. **133**, A97 (1964).
[39] A. A. Kopasov and A. S. Mel'nikov, Phys. Rev. B **101**, 054515 (2020).
[40] P. San-Jose, C. Payá, C. M. Marcus, S. Vaitiekėnas, and E. Prada, Phys. Rev. B **107**, 155423 (2023).
[41] D. Razmadze, E. C. T. O'Farrell, P. Krogstrup, and C. M. Marcus, Phys. Rev. Lett. **125**, 116803 (2020).
[42] A. Ibabe, M. Gomez, G. O. Steffensen, T. Kanne, J. Nygard, A. L. Yeyati, and E. J. H. Lee, Nat. Commun. **14**, 2873 (2023).
[43] A. Vekris, J. C. Estrada Saldaña, J. de Bruijckere, S. Lorić, T. Kanne, M. Marnauza, D. Olsteins, J. Nygård, and K. Grove-Rasmussen, Sci. Rep. **11**, 19034 (2021).
[44] A. Bringer and T. Schäpers, Phys. Rev. B **83**, 115305 (2011).
[45] Y. Tserkovnyak and B. I. Halperin, Phys. Rev. B **74**, 245327 (2006).
[46] T. Richter, C. Blömers, H. Lüth, R. Calarco, M. Indlekofer, M. Marso, and T. Schäpers, Nano Lett. **8**, 2834 (2008).
[47] G. W. Holloway, D. Shiri, C. M. Haapamaki, K. Willick, G. Watson, R. R. LaPierre, and J. Baugh, Phys. Rev. B **91**, 045422 (2015).
[48] J. Cayao, A. M. Black-Schaffer, E. Prada, and R. Aguado, Beilstein J. Nanotechnol. **9**, 1339 (2018).
[49] C. W. J. Beenakker and H. van Houten, Phys. Rev. Lett. **66**, 3056 (1991).
[50] A. Furusaki, H. Takayanagi, and M. Tsukada, Phys. Rev. B **45**, 10563 (1992).
[51] J. C. Cuevas and F. S. Bergeret, Phys. Rev. Lett. **99**, 217002 (2007).
[52] A. A. Abrikosov, Sov. Phys. Usp. **12**, 168 (1969).
[53] S. Skalski, O. Betbeder-Matibet, and P. R. Weiss, Phys. Rev. **136**, A1500 (1964).
[54] I. Sternfeld, E. Levy, M. Eshkol, A. Tsukernik, M. Karpovski, H. Shtrikman, A. Kretinin, and A. Palevski, Phys. Rev. Lett. **107**, 037001 (2011).
[55] N. Shah and A. Lopatin, Phys. Rev. B **76**, 094511 (2007).
[56] V. H. Dao and L. F. Chibotaru, Phys. Rev. B **79**, 134524 (2009).
[57] G. Schwiete and Y. Oreg, Phys. Rev. B **82**, 214514 (2010).
[58] J. Cayao, P. San-Jose, A. M. Black-Schaffer, R. Aguado, and E. Prada, Phys. Rev. B **96**, 205425 (2017).